3

Computer-aided Analysis and Interpretation of HRCT Images of the Lung

Zrimec Tatjana[1] and Sata Busayarat[2]
[1]*Centre for Health Informatics*
[2]*School of computer science and engineering Wales, NSW 2052*
University of New South Wales
Australia

1. Introduction

High Resolution CT (HRCT) techniques developed in the last decade have become invaluable tools for the detection of subtle diffuse lung disease patterns and for their characterisation into multiple possible diseases. HRCT imaging protocols produce 3D volume data and enable accurate visualisation of imaged anatomy and much better visualisation of the disease patterns than conventional X-rays. However, the amount of information produced by today's HRCT scanners is beyond the ability of a radiologist to process in normal clinical practice. Single detector scanners generate up to 40 images per study and multi-slice detectors generate 300-600 high-resolution axial images. Furthermore, the number of images is rapidly growing. It is difficult and time consuming to analyse images accurately and efficiently by hand. Systems for computerised image analysis are needed to help with the large number of images and to draw radiologist's attention to fewer, diagnostically useful images.

The goal of computerised medical image analysis and interpretation is to detect abnormal appearance of the imaged anatomy and to assist radiologists in identifying and integrating all the useful information available in an image (Brown & McNitt-Gray, 2000). There is a growing number of computer-aided diagnosis (CAD) systems aimed at automating the analysis of lung CT images and supporting diagnosis (Uppaluri, et al., 1999; Uchiyama et al., 2003; Sluimer, 2005; Zrimec et al., 2007; Tolouee et al., 2008). Uppaluri *et al.* (1999) presented a CAD system for detecting six lung tissue patterns using textural features. A multiple feature method was used to determine the optimal subset among 22 textural features calculated for each 31x31 pixel square region of interest in an image. A Bayesian classifier was trained to use the optimal subset of features to recognize six different tissue patterns. They reported that the automated system performed as well as experienced human observers who were told the diagnosis in advance. Uchiyama et al. (2003) also divided the lung into square regions and employed neural networks to perform classification of HRCT images into six textural classes. The neural network, trained with examples of different tissue patterns, was able to automatically detect images containing abnormalities and to provide good classification. In the work reported by Sluimer (2005), a multi-scale filter bank was used to represent the local image texture and structure. They used various classifiers to

train the system. They reported that the CAD ROC curve showed very similar performance compared to that of two radiologists.

Various combinations of wavelet transforms, in combination with support vector machines (SVM's), were also used to discriminate among several texture patterns from patients affected by interstitial lung diseases. Two sets of over-complete wavelet filters, discrete wavelet frames (DWF) and rotated wavelet frames (RWF) were used to extract the features, which best characterise the lung tissue patterns (Tolouee et al., 2008). The system was able to successfully classify four different lung patterns with the best multi-class accuracy achieved when combining DWF and RWF. Depeursinge (2010), described a texture classification system based on discrete wavelet frames (DWF) and quincunx wavelet frames (QWF) together with grey level histogram (GLH). After testing the performance of five different classifiers from the Weka machine learning environment (Witten & Frank, 2005), it was shown that the SVM classifier was the best in companions to Naive Bayes, k-NN, J48 and Multi Layer Perceptron (MLP), for correctly classifying instances into six classes of lung tissue patterns (Depeursinge, 2010).

Almost all existing CAD systems divide the image into small, usually square regions, applying classical image processing techniques to calculate the image features. They do not take advantage of existing anatomical knowledge. Accurate interpretation of medical images requires a detailed understanding of normal lung anatomy and of pathological changes that occur in the presence of disease (Webb *et al.*, 2000). In our approach to computer-aided detection, we first segment and extract anatomical features and landmarks from the images and then use them to help detecting abnormalities caused by disease processes. This approach enabled us to develop, for the first time, a digital model of the lung anatomy that incorporates regional information crucial for correct diagnosis. This is particularly important for lung diseases because the same disease patterns located in a different region of the lung or distributed in a different way can be linked to different pathologies (Webb *et al.*, 2000). Lung regions are extensively used in clinical reporting for indicating the location of detected disease patterns.

This chapter presents a methodology for building a computer system for interpreting HRCT images of the lung. The system is aimed at:

- automating the analysis and understating of lung CT scans,
- detecting lung disease patterns associated with diffuse lung diseases,
- providing radiologist with Computer-Aided Diagnosis as a second opinion.

To achieve these goals, the system is required to perform image analysis and interpretation, which includes:

a. *Segmentation* of the organs of interest;
b. Detection, classification and labelling of possible disease patterns;
c. Combination of disease patterns into a list of *differential diagnosis*.

Segmentation in image processing is defined as the separation of an image into regions that are meaningful for a specific task (Sonka, 2000). It is one of the first steps leading to image analysis and interpretation. In medical imaging, the segmented regions usually refer to organs, such as the heart, liver or lungs, or disease patterns, such as brain tumours or fibrosis in the lungs. Different image segmentation algorithms are used deepening on the type of object or feature of interest. Image segmentation usually involves image normalisation or pre-processing and low-level image processing to segment regions of interest from the image. Each region can be one to several pixels in size. It often involves

higher-level candidate selection or ranking, where domain knowledge about the segmented object is used. In medical imaging, such knowledge can be about the anatomy or the specific disease patterns. The low-level image processing, often used in segmentation, includes thresholding, region growing, connected-component labelling, and mathematical morphology. Good descriptions of segmentation methods can be found in image processing text books (Gonzalez & Woods, 1993, Shapiro & Stockman, 2001) or books that are specific to medical image segmentation, such as (Sonka, 2000, Suetens, 2008). In this chapter we present our knowledge-based approach to segmentation lung anatomy and other anatomical landmarks. We also present the way in which the landmarks are used for generating regional information needed for image interpretation.

Detection, classification and labelling of possible disease patterns are the major tasks of the system and often are performed iteratively to achieve satisfactory results. There is a large class of disorders known as Diffuse Parenchymal Lung Disease (DPLD) that primarily affect the lung parenchyma and can be best diagnosed using HRCT. They are characterised by specific abnormal findings mostly texture-like in appearance (Webb, Muller & Naidich, 2000). Consequently, most of the systems for computerised analysis of HRCT images of the lung are texture based and are trained to detect and classify abnormal tissue patterns into several textural categories. The system for computer-aided interpretation of HRCT images, presented here, differs from existing systems by using knowledge about the disease patterns, their appearance and distribution, in addition to texture information. The rules for classifying detected patterns are automatically generated using machine learning. Two examples of pathology detection are presented to demonstrate the different detection techniques required for different disease patterns.

Differential diagnosis (DDx), the process of weighing the probability of one disease versus that of other diseases, is a particularly challenging task even for experienced radiologist since the combination of several abnormal findings can be associated with a specific diagnosis (Webb *et al.*, 2000). It requires good detection of disease patterns and substantial experience in radiology. Consequently, there is a relatively small number of publications on this topic. We present our preliminary results on differential diagnosis.

2. High-resolution CT and the human lung

Detailed understanding of lung anatomy is a prerequisite for successful image interpretation. We will look at the lung anatomy and it appearance on HRCT images. We will also learn what is used for image interpretation by radiologists.

2.1 Lung anatomy

There are two lungs, one on each side of the thoracic cavity, which are protected by the rib cage. Between the two lungs lies a space called the mediastinum, which is occupied by the heart, the trachea (the main airway), the oesophagus (tube to the stomach) and large blood vessels. In healthy people, each lung is elastic and conical in shape (Figure 1a). The hilum is the area on the medial surface of each lung, where the main bronchus, pulmonary artery, pulmonary vein and nerves enter and leave the lung. Each lung has a major or oblique fissure that divides the lung into upper and lower lobes. The right lung has also a minor or horizontal fissure that further divides the upper lobe. The lung consists of bronchi (or pulmonary airways), pulmonary blood vessels and connective tissue that support the structure of the lung; together these are called parenchyma. The pulmonary-arterial and the

bronchial trees run alongside each other and branch simultaneously in a tree-like structure. The branches are of similar size in a healthy lung.

2.2 High-resolution CT images of the lung

Computer tomography (CT) is currently the best imaging modality for diagnosing lung diseases. High resolution CT scanners generate a three dimensional view of the imaged organs with sub-millimetre resolution in axial sections. It provides detailed information regarding the lung parenchyma and can delineate structures down to the level of the secondary pulmonary lobule, the smallest structure in the lung. It is particularly useful for image-based diagnosis, since alteration of the lung anatomy, caused by a disease, can be clearly seen in a thin-slice CT image (Webb et al., 2000). Figure 1 shows examples of a lung (a), an HRCT series of axial images (b) and an axial image with normal anatomy (c).

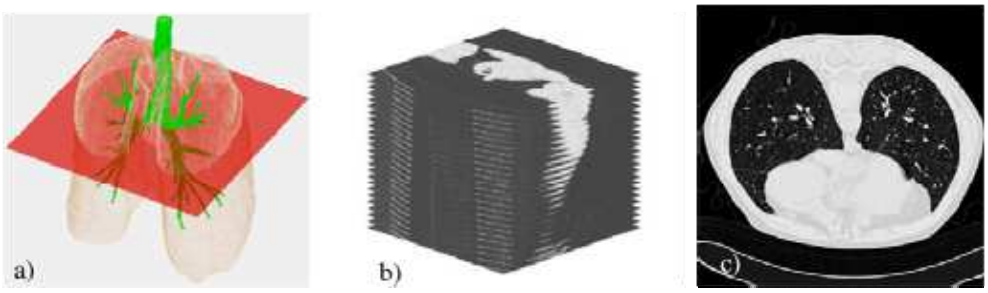

Fig. 1. Examples of a human lung (a), a series of HRCT images (b) and an axial image with normal anatomy (c).

In patients with diffuse lung disease, contiguous scanning is usually not necessary, since diffuse lung abnormalities can be adequately sampled with the acquisition of interspaced sections (Muller, 1991). In a routine HRCT protocol, 1 mm thick images are acquired with 10 to 20 mm inter-slice spacing.

To develop and evaluate our system, HRCT scans from three radiology practices in Sydney, Australia were used. The images were taken using a SIEMENS CT scanner with a tube voltage of 140kVp, current between 180 and 280 mAs, and exposure time of 750 ms. Data were reconstructed as 512x512 matrices with a slice thickness of 1.0 mm and 15 mm inter-slice spacing. The data are stored as DICOM 16-bit greyscale images with the pixel intensity proportional to tissue density represented in Hounsfield Unit[1] (HU).

2.3 Image marking and semantic labelling

We use machine learning to train a computer to recognise disease patterns in an HRCT image and to correctly classify them into different diseases. Supervised learning requires examples of lungs with labelled disease patterns and areas with normal appearance. Although the disease patterns are clearly visible to a trained human eye, it is not obvious how to provide an appropriate description that can be used by a computer. To enable easy

[1] Hounsfield unit (HU) is a unit used in medical imaging (CT or MRI scanning) to describe the amount of x-ray attenuation of each "voxel" (volume element) in the three-dimensional image.

communication with the radiologists while acquiring knowledge about different disease appearance in the HRCT images, we used a web-based interactive tool for image labelling.
The LMIK image labeller, developed for the Learning Medical Image Knowledge project (Rudrapatna *et al.*, 2004), was designed for easy access, marking and semantic labelling of images. It automatically downloads images from a hospital picture archiving and communication system (PACS) and stores them in a local LMIK database. The web-based interface enables access to the image database, provides interactive image display and a variety of semantic labelling facilities. Radiologists are able to remotely access cases from the local database, select and delineate representative examples of different lung diseases patterns (see Figure 2).

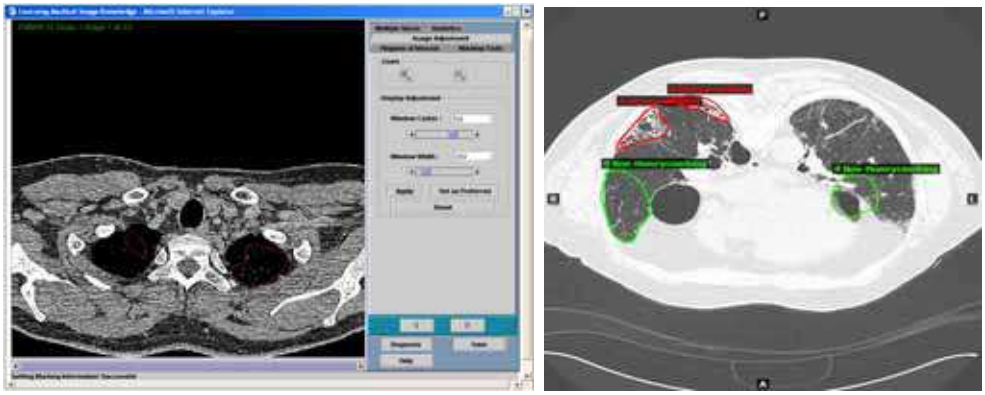

Fig. 2. LMIK Image labeler for Web-based semantic marking and labeling.

Every marked example consists of a delineated region of interest (ROI) containing a pattern, a label indicating the name of the pattern and the pattern severity, ranging from normal, moderate to severe.
The LMIK image labeller was used to provide ROIs with disease patterns as well as ROIs with normal lung tissue by at list two radiologist for the same cases. Radiologists were also able to compare their marking and labelling with each other and to agree on consistent marking for some difficult cusses.

2.4 Observing radiologists interpreting HRCT images

We had three experienced radiologist in our project group. They provided us with the latest textbooks and the books they are using when reporting on images (Webb *et al.*, 2000) as well as multimedia educational tools for interpretation of HRCT images of the lung,. We also had a few sessions observing the radiology reading and reporting HRCT cases in radiology practice.
The information used in the interpretation process can be summarised as:

a. knowledge of the imaged anatomy being investigated
b. landmarks
c. regional descriptions

Knowledge of the imaged anatomy being investigated – Radiologists use knowledge of anatomy when inspecting HRCT images. For example, knowledge about the shape of the lung in a cross sectional HRCT image helps to understand which part of the lung is captured in the

image or knowledge of a broncho-arterial pair appearance helps to detect the presence or absence of a bronchial disease.

Landmarks – Radiologists make extensive use of anatomical landmarks, which are objects or features that help determine the location of the imaged part of the body. Selected landmarks are usually consistent, despite variations in the patient's position during scanning, or changes due to disease progression (Betke *at al*, 2003).

Regional descriptions – Knowledge of the regional distribution of lung diseases also assists in detecting pathology. In textbooks on interpreting HRCT images of the lung, it is noted: "When attempting to reach diagnosis using HRCT, the practitioner should not only be focused on the morphology of the structures appearing in the HRCT, but on their distribution, location and appearance" (Webb *et al.*, 2000). Many lung diseases show specific regional distributions or preferences. The same features located in a different region of the lung or distributed in a different way can be linked to different pathologies (Webb *et al.* 2000). Preferential predominant involvement of one or more lung regions is commonly seen in HRCT, even in patients with chest radiographs showing a "diffuse" abnormality (Muller, 1999). For the purpose of interpreting HRCT the regional distribution can be categorised in several ways:

- central lung vs. peripheral lung
- upper lung vs. lower lung
- anterior lung vs. posterior lung
- unilateral vs. bilateral.

2.5 Knowledge based analysis of HRCT images of the lung

To take advantage of the wealth of medical knowledge in lung image analysis, a computerised lung model or atlas, depicting the lung anatomy and lung appearance on the HRCT images is required. In the absence of such a model, we built a digital model from a nearly normal case of HRCT images taken with contiguous scanning, i.e., without inter-slice spacing, to represent the structure and anatomy of the lung and to record regional information. Literature on the visual interpretation of HRCT images of the lungs (Webb *et al.*, 2000) was used to acquire knowledge and create rules about disease appearance and behaviour. Machine learning was employed to automatically generate rules for detecting anatomical features and disease patterns during image analysis.

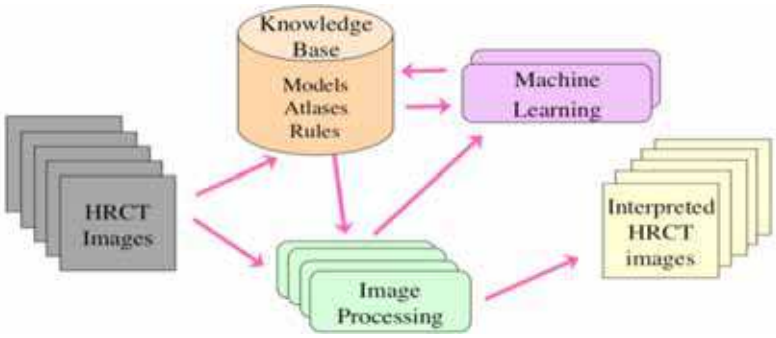

Fig. 3. System overview. Images are processed and interpreted using image processing algorithms, adapted for medical images, and knowledge that is mostly automatically generated and stored in the knowledge base.

An overview of the main modules involved in the computer aided detection and interpretation system is shown in Figure 3. An example of the use of the knowledge base is in providing spatial constraints indicating where an algorithm should be applied and semantic constraints to segment the correct objects. The knowledge includes a lung model, several HRCT lung atlases and a set of heuristic rules. The image processing module contains a variety of image processing algorithms that are able to work in cooperation with the knowledge from the knowledge base. The image processing module together with the machine-learning module are used to generate new knowledge that is stored in the knowledge base.

3. Segmentation of lung anatomy

Segmentation in medical imaging is particularly challenging largely because the appearance of organs and diseases differ from person to person. Other factors, such as acquisition artefacts, poor image quality or different scanning protocols, also make the task nontrivial. For automated segmentation to be successful, image processing needs to incorporate domain-specific knowledge as used by radiologist.
The set of anatomical features segmented by our system are grouped into:

- *Lung segmentation* – this includes features that help determine the lung structure, for example, lung boundaries, fissures;
- *Segmentation of broncho-vascular structures* – features that are part of the normal lung anatomy, for example, airways and vessels;
- *Landmarks segmentation* – this includes features within the lung and the lung surroundings, for example, the trachea and the ribcage.

3.1 Lung segmentation

Segmenting the lung fields is the primary task in any CT pulmonary image analysis. Automated and semi-automated segmentation of CT and HRCT has been an active area of research over the past decade. Armato and Sensakovi (2004) emphasised the importance of lung segmentation as a pre-processing step of a CAD system. Similarly, the bronchial tree is one of the most important and most prominent structures inside the lung. Kuhnigk *et al.* (2005) recognised the importance of the bronchial tree segmentation as a way to divide the lung lobes into smaller regions and use them to evaluate the distribution of diseases.
A number of authors have reported high accuracy for segmenting lung fields. Most of those approaches are based on grey-level thresholding, seeded region or volume growing or a combination of both. Examples that fall into this category are (Brown, et al., 1997; Hu, Hoffman, & Reinhardt, 2001; Garnavi, *et al.*, 2005; Sluimer, 2005; Lee, et al., 2004). Various techniques were used to overcome shortcomings of the basic thresholding and region growing algorithms. Another approach uses active contouring such as energy-minimising snakes to find the lung contour, for example (Papalousis, 2003; Li & Reinhardt, 2001). Active contours have a better ability to deal with irregular shapes than thresholding and region growing (Kass *et al.*, 1987). This is because they use their own shape as an input, instead of the pixel intensity alone.
In lung segmentation 3D lung surfaces and 2D lung boundaries are determined to separate the pixels belonging to the lung parenchyma from the background. Some issues need addressing when segmenting the lungs on 2D cross-sectional images. First, the two lungs are close to each other in the posterior part of the body and a simple thresholding or

morphology method often connects the two lungs. Merged lung need to be separated to determine the left and the right lung. The second issue is that segmentation sometimes includes the main bronchi as part of the lung since the bronchi also have low intensity and enter the lung in the hilum region. Main bronchi are generally not considered part of the lung and they also create irregularities in the hilum surface. The last issue occurs in the anterior part of the lung. Gas in the stomach also appears as a low density region on the image so the segmentation often includes it as part of the lung as well.
A method for automatic lung boundary segmentation, described here, addresses all the above-mentioned issues. It uses a combination of the thresholding and morphology operators followed by active contours to achieve both robustness and smooth contour. Lung segmentation consists of the following steps:

- *Pre-processing* – reduces noise and removes the large bronchi and CT background.
- *Segmentation* – extracts the lung from the image using a combination of thresholding, morphology and other image processing techniques.
- *Post-processing* – ensures the two lungs are separate, removes remaining false-positives and smoothes the contour using active contour snakes.

3.1.1 Pre-processing

The number of noisy pixels in an HRCT image may vary depending on the CT machine and the parameters used. A 3×3 median filter is used to reduce the noisy pixels by averaging them with the 3×3 neighbouring pixels. Even though the sharpness decreases as a result of the median filter, its effect is insignificant for large objects like the lungs. The large bronchi are segmented and removed from the image to prevent inclusion in the lung boundary.

3.1.2 Segmentation

Thresholding generally works well for lung segmentation because of the great intensity difference between the lung and the surrounding tissues in the thorax. Initially, a fixed threshold of −500 HU (middle point between air and water density) was used, but it was found inappropriate for some special cases. In some lung diseases, the density range of lung parenchyma is wide so a fixed threshold may not be optimal in all cases. Consequently, a histogram analysis is used to select a threshold. After removing the CT background, the

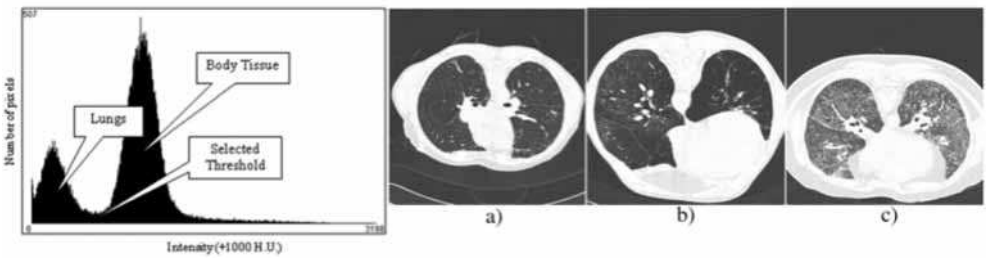

Fig. 4. Intensity histogram of an HRCT image of the lung. The first peak corresponds to low intensity pixels in the lung and the second peak corresponds to high-intensity pixels in the body. The threshold used for lung segmentation is the midpoint between the two peaks. Lungs with different densities: normal density lungs (a), low-density lungs (b) and high-density lungs (c).

intensity distribution of an HRCT image is bimodal, as shown in the histogram in Figure 4. The first peak in the histogram corresponds to pixels inside the lungs and the second peak corresponds to the pixels in the body tissue. The threshold selected for lung segmentation is the midpoint between the two peaks, ensuring that most of the pixels in the two groups are correctly separated.

In some high-density disease cases, the lung may be broken into multiple regions after thresholding. A sequence of morphological operators is applied to smooth the lung contour and to merge multiple regions into one large region.

3.1.3 Post-processing

A special strategy is used to address the issue of two connected lungs (see Figure 5). After the thresholding and morphology, the following heuristic rule is applied to test whether the two lungs are merged:

If

there is only one segmented object **and**
its size is over 1220 mm^2 **and**
its centre-of-mass lies within 40 mm width from the image centre line

then the lungs are merged

The lung pleura are used to help separate the lungs. The lung pleura are thin layers of membrane covering the lungs. While the pleura have the same density as other tissues, their intensity on HRCT is lower because of the HRCT volume-averaging effect. As a result, the pleura line separating the two lungs is often not detected by the globally optimal threshold. A threshold of −750 HU is used to segment the pleural line lying between the spinal cord and the sternum, as shown in Figure 5(c). The detected pleural line and the final result is shown in Figure 5(d).

Active Contour Models, or snakes, are used as the final post-processing step to smooth the lung contour. Snakes are dynamic, energy minimising curves, first introduced by Kass *et al.* (1987). A snake is a special form of deformable model, which is moved under the influence of internal forces and the curve itself, and external forces calculated from the image data. Generally, the internal force discourages bending the curve and the external force potentially pulls the curve toward the image contour. The deformation of snakes is

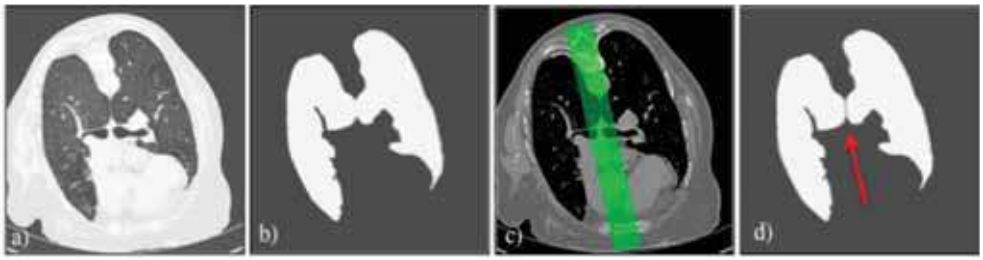

Fig. 5. An image of two lungs that are close to each other: appearance on HRCT (a), and the merged region resulted from the thresholding and morphology during the segmentation (b). The potential lung touching area, the 60-pixel-witdh bar between the spinal cord and the sternum (c), and the two lungs separated, indicated by the arrow, using the detected plural line (d).

controlled by an energy function that incorporates the internal and external forces and defines their weights. More specifically, the energy function is defined as:

$$E = \int_c \alpha(s)E_{cont} + \beta(s)E_{curv} + \gamma(s)E_{image}ds \quad (1)$$

where the contour, *c*, is parameterised by its arc length, *s*. The first two terms define the internal energy and the last term defines the external energy. The coefficients α(*s*), β(*s*), and γ (*s*) are user-defined constants used to balance the smoothness and fitness of the contour. Normal Push force proposed by Papasoulis (2003) helps push the snakes into a concavity, which is common in lung contours near hilum. The snakes are initialised to be two circles centred at the centroids of the two lungs. The circles' radii are determined by the size of the lungs. The circles are clipped so that they do not lie outside the image. The entire deformation requires up to 200 iterations but the algorithm may stop early if no change occurred during the last iteration. Figure 6 shows intermediate steps and the final result of the lung segmentation.

3.2 Fissure segmentation

Fissures divide the lung into lobes that are relatively independent functional units. Lung pathology may be confined to one lobe, which in some cases can be surgically removed. There are several reports on segmenting pulmonary fissures. A method described by Kubo, et al. (2001) used a linear detector to segment fissures from thin CT scans and used surface curvature calculation and morphology filters to improve the results around pulmonary lesion. A fuzzy set approach with a fixed threshold was used by Zhang and Reinhardt, (1999) to segment the fissures. Wang *et al.* (2006) proposed a method for fissure segmentation using a 2D-shape-based curve-growing model with a semi-automatic initialisation.

Fig. 6. Results of lung boundary pre-processing at various steps: an input lung HRCT image (a), after large bronchi removal (b), after non-body pixel removal (c) and final result (d).

A knowledge-based method for fissure detection, developed in our previous work, performs well in cases where fissures are fully visible (Zrimec & Busayarat, 2004; Zrimec *et al.*,2004). However, in almost 30% of the images, the fissures are only partially visible or are not visible at all (Eenakshi *et al.*, 2004). Using information from the lung model, it was possible to successfully determine fissures in the cases where fissures were partially visible or missing. The model guided fissure detection by predicting its expected location. The detected fissures were used to determine the lung lobes in 2D images (see Figure 7(a) and (b)) and in 3D models of patient data (see Figure 7(c)).

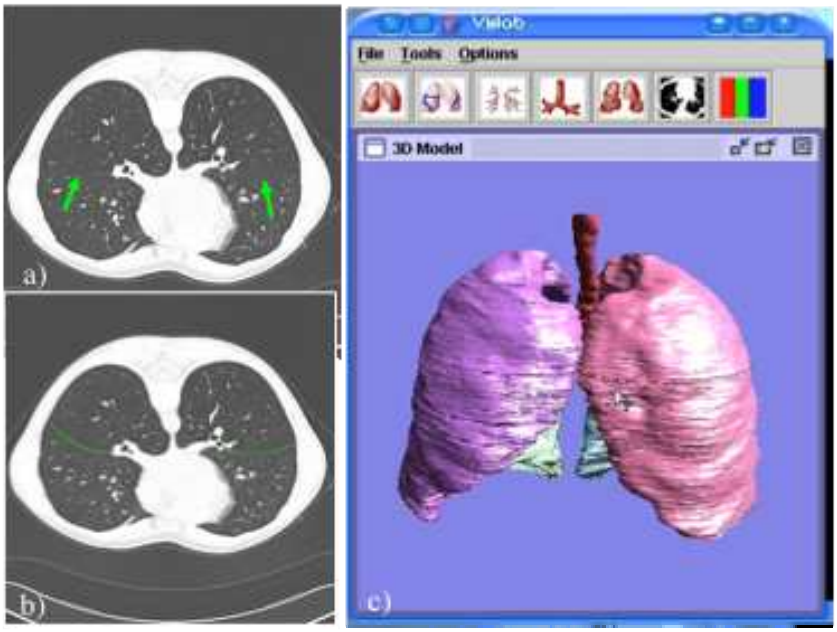

Fig. 7. Majors fissures visible on both lungs, (arrows) (a), segmented fissures (b) and a 3D model with four lung lobes (c).

3.3 Segmentation of broncho-vascular structures

Pulmonary airways, or bronchi, are amongst the most important structures in the lungs. They distribute inhaled air to the alveoli where oxygen and carbon dioxide exchange between air and blood takes place. The bronchial tree is complemented by a system of arterial blood vessels and pulmonary veins that transport the blood. From a clinical point of view, the identification of bronchi CT images provides valuable clinical information in patients with suspected airways diseases including bronchiectasis and constrictive obliterative bronchiolitis (Webb *et al.*, 2000). One of the main signs of a respiratory disease is the dilation of the bronchi. From an image processing point of view, bronchi can be used as landmarks for image registration, because their branching pattern is relatively static for the first four generations (Tschirren *et al.*, 2002).

Several publications discuss segmentation of bronchi in HRCT. Because the bronchi exhibit a tree-like structure, 3D approaches such as volume growing or tree-skeleton detection have been employed (Chiplunkar, et al., 1997; Aykac, et al., 2003). Their method was based on a 2D segmentation using an eight-connected seeded region growing with an adaptive threshold and a 3D connectivity analysis. The work was extended to be capable of determining the bronchial tree skeleton, detecting the branching points and matching them (both intra and inter-subject). A group from France also reported research on bronchial tree segmentation (Preteux, Fetita, & Grenier, 1997; Fetita & Preteux, 1999; Fetita & Preteux, 2000; Fetita & Preteux, 2001). Their method also consisted of 2D segmentation and 3D analysis of the 2D results. Their 2D segmentation was based on the connection cost algorithm, which filled all the local intensity minima (i.e. bronchi lumens). The 3D analysis involved stacking

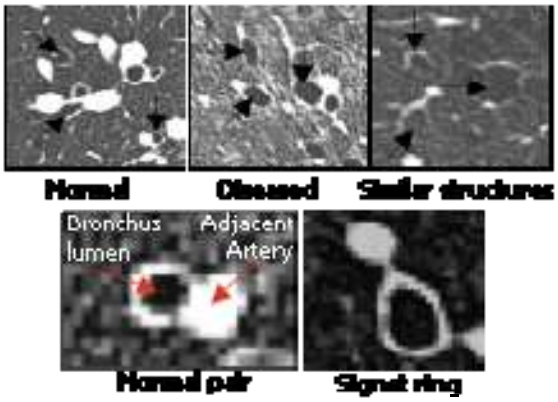

Fig. 8. Broncho-vascular pairs. Top left: an example of normal boncho-vascular structure, top middle: an example of diseased boncho-vascular structure with enlarged bronchi, top right: structures within the lungs with similar appearance; left bottom: enlarged pair; right bottom: an example of bronchial dilatation – "signet ring".

the 2D segmented results and filling up the gap where a bronchus is missing. They also constructed a 3D descriptive structure of the bronchial tree from the 3D stack.

In axial cross-sectional images, vertically oriented bronchi appear as high-attenuation circular or elliptical rings. Radiologists usually use this type of bronchus for diagnosing airway diseases, such as bronchiectasis. Figure 8 shows examples of a normal broncho-vascular pair and an abnormal pair with dilated bronchus. Automatic identification of bronchi, running nearly perpendicular to the scan plane, consists of potential candidate generation and candidate classification based on knowledge in the lung model. After thresholding, edge and radius analysis is performed to find all potential bronchi candidates, all dark rounded objects with bright walls. P-tile thresholding was used to handle inter-subject lung tissue density variability. Each object in the candidate bronchi list is represented by nine attributes. Knowledge of bronchial appearance in HRCT images is used to derive a heuristic function for ranking the candidates. The knowledge includes their average intensity, size, shape and position. Knowledge from the lung model, which includes a fully segmented bronchial tree, provides the expected number of bronchi for each lung in each cross-sectional image. The heuristic function, which is a weighted sum of all attributes, is used to remove all objects that are not bronchi. The final segmentation of the bronchi is done by region growing and rule-based classification to distinguish bronchi from other structures with similar appearance (Busayarat et al., 2005a).

Each bronchus has an accompanying artery. The arteries appear as high-attenuation solid circles or ellipses. An automatic method for detecting arteries based on (Chabat, et al., 2001) had problems with the ambiguous appearances of the adjacent arteries, which presents difficulties even for an experienced radiologist. It also had problems in providing accurate measurements of the size of small arteries due to the pixel rounding effect. A new technique was developed that uses knowledge-directed template matching to approximately locate the adjacent artery (Busayarat et al., 2005b). Knowledge of broncho-arterial anatomy helps locate the adjacent artery when there is more than one possible candidate nearby. Even though there is a high contrast between artery and lung

parenchyma, an artery often contacts with other similar-density structures, such as bronchial wall and other vessels. This causes the growing region to leak into those structures. A specially developed region-growing algorithm, with leak correction, was used to accurately segment the arteries and to calculate their sizes. In contrast to other template matching techniques, where predefined templates are used, here the templates are generated on the fly using the detected bronchi in an image.

3.3.1 Trachea segmentation and carina detection

The trachea appears in an axial slice as a circular black object located in the middle of the body contour. To segment the trachea in an HRCT image, a fixed value of -400HU threshold is applied. After morphological filtering and connected component labelling, the trachea is segmented using knowledge about its expected location and size. Since the oesophagus can sometimes be misclassified as the trachea, the rules for trachea segmentation also include knowledge about the appearance of the oesophagus. The trachea is traced until the point at which it starts to bifurcate into two main bronchi. This bifurcation is known as carina (Figure 9). In a sparse scan (with 15 mm gap between consecutive slices), the exact location of the carina may not be visible. In that case, the slice before the trachea bifurcation is used as the carina position. We use carina as a landmark.

3.4 Detecting lung landmarks

Anatomical landmarks that are used to help determine the location of the imaged part of the lung include landmarks that are located on the ribcage and landmarks that are part of the lungs. The sternum, vertebrae and spinal canal are located on the ribcage. The trachea bifurcation - carina, hilum and the lung root are part of the lungs. These landmarks are often consistent and stable even in a presence of a disease. For example, the sternum and the vertebrae are good anatomical landmarks because they are bones and their position is relatively fixed within the chest. The sternum and the vertebrae have been used before for a different task, namely for inter-patient image registration (Archip, *et al.*, 2002; Betke, *et al.*, 2003). Radiologists use the carina, the bifurcation point of the trachea and the hilum, as a landmark. The hilum, as a landmark, defines the base of the lung, which is comparable between patients. Figure 9 shows examples of the landmarks.

Archip *et al.* (2002) used a knowledge-based approach to identifying the spinal cord. The knowledge base consists of an anatomical structures map and a task-oriented architecture, which is represented by a frame-like system. Deglint *et al.* (2007) uses a different approach to segment the spinal cord, based on 3D-seeded region-growing to detect the bones. The initial seed voxels are automatically obtained by an image processing procedure. The Hough transform is then applied on each image to find the best fitting circle inside the backbone, which represents the spinal cord. Betka *et al.* (2003) used an attenuation-based template matching approach to detect the sternum and spine. The sternum and spine were used to compute the optimal rigid-body transformation that aligns two CT scans of the same patient.

3.4.1 Sternum segmentation

The sternum and the spine are good landmarks in the chest HRCT images because they are bones outside the lungs. Their density (~1000 HU) is significantly higher than the surrounding soft tissue (30 to 40 HU) so they are relatively easy to segment. The spinal cord

is inside the spine and because of its smaller size, provides an accurate landmark. Figure 9(a) shows HRCT appearances of the sternum, spine and spinal canal.

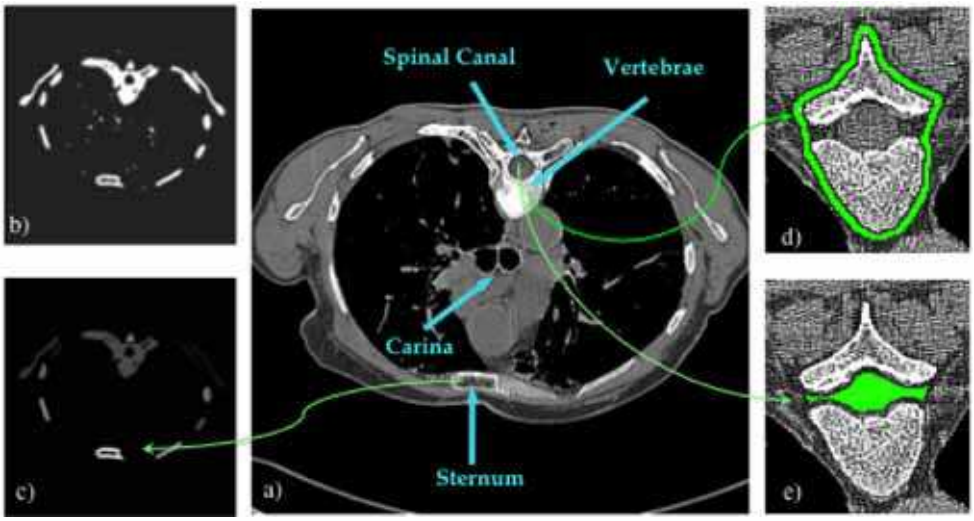

Fig. 9. HRCT appearances of carina, sternum, vertebrae and spinal canal (a); Segmented bones, sternum candidates (b), Segmented sternum (c); Segmented vertebrae using snakes (d) and segmented spinal canal (e). The image (a) is displayed using soft-tissue window setting (mean=40, width=500).

Our method uses intensity-based thresholding and morphological operators to segment the bones. A simplified version of the knowledge base presented in (Archip, et al., 2002) is also used to distinguish the sternum and the spine from other bone structures. The knowledge, encoded as parameters in the image processing script consists of knowledge about the sizes of the sternum and spine and their approximated positions, relative to the body. Once the spine is detected, a template-matching method is used to search for the spinal cord inside it. Sternum segmentation starts by removing the pixels outside the body in the image. Next, thresholding is used to segment bony pixels in the image. The bone density ranges from 400 HU, which is significantly higher than the surrounding soft tissues. The threshold value chosen for segmenting bone pixels is 300 HU, which is low enough to compensate the partial volume effect, and high enough to not include the tissues. Binary dilation and connected-component labelling are then applied to separate each bony region and remove noise. Every connected region that is smaller than 50 pixels is considered noise and removed from the image. The remaining connected regions are candidates for the sternum selection during the post-processing step. An example of an image with all candidates is shown in Figure 9(b).

In the post-processing step, knowledge of the location of the sternum is used for candidate selection. Specifically, the expected location of the sternum is near the middle and anterior part of the body. This is represented as a distance between the candidate sternum and the body. The Manhattan or city-block distance, between the candidate midpoint and the middle and most anterior point of the body-bounding box, is used to rank the candidates using Equation 2:

$$sternum\_distance(C,B) = \left|mid_x(C) - mid_x(B)\right| + \left|mid_y(C) - \max_{p\in B} p_y\right|$$
$$mid_{axis}(obj) = \frac{\min_{p\in Obj} p_{axis} + \max_{p\in Obj} p_{axis}}{2} \quad (2)$$

where B and C are sets of pixels belonging to a candidate and the body region, respectively. The candidate with the lowest distance is selected is the sternum (Figure 9(c)).

3.4.2 Spine and spinal cord segmentation

The spine detection algorithm is almost identical to the sternum segmentation algorithm because they are both bones and their locations can be assumed. The obvious difference is the location constraint because the spine appears in the posterior whereas the sternum is in the anterior part of the body. Therefore, the distance function is changed to Equation 3.

$$spine\_distance(C,B) = \left|mid_x(C) - mid_x(B)\right| + \left|mid_y(C) - \min_{p\in B} p_y\right| \quad (3)$$

One problem with spine detection is that it sometimes connects with the rib. We overcome this problem by removing all pixels that are further from the component's middle axis than the empirically determined distance of 37.5 millimetres. We set the upper limit of a spine diameter to be 75 millimetres using the guideline from Madden (2001). The spine outline is defined using active contour snakes. The snake is required because the spinal cord is not always completely surrounded by bones. The snake wraps around the spine and makes it a close-shape object (see Figure 9(d)). The snake is configured to rely more on the internal elastic and bending forces, than the external imaging force.

For segmentation, we defined the spinal cord's appearance in HRCT as the biggest circular and low-density object inside the spine (Figure 9(e)).

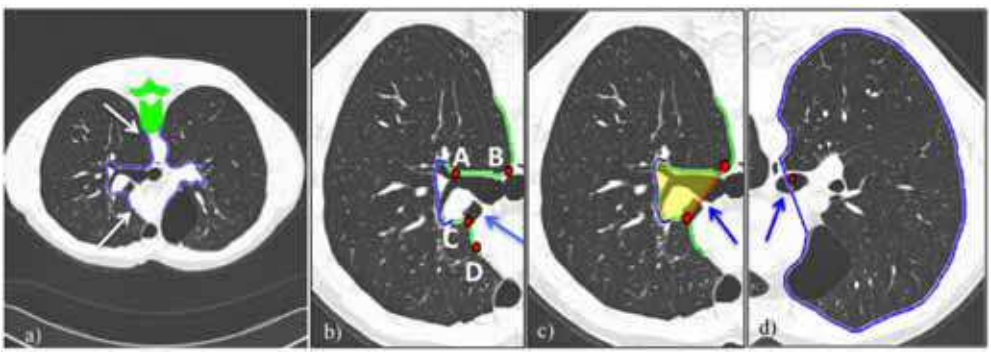

Fig. 10. The mediastinal part of the lung with potential hilum regions (white arrows) (a); candidates for hilum end points (b), detected hilum (arrow) (c); lung root (arrow) (d).

3.5 Hilum detection

The hilum is a wedge-shaped depression of the mediastinal surface of each lung, where the bronchi, blood vessels, nerves, and lymphatics enter or leave the viscus (Webb *et al.*, 2000).

On axial HRCT images, the hilum appears in the mediastinum as a high-density hole surrounded by low-density lung parenchyma. It can be used as an anatomical landmark in many applications, such as lung region separation and image registration.
The method for hilum detection is based on curvature analysis of the lung boundaries and proceeds as follows. To restrict the curvature analysis, a potential hilum region is determined (see Figure 10(a) marked with arrows). The hilum region is only the mediastinal part of the lung boundaries. A curvature analysis is performed in that region to detect the most concave curved section of the lung boundaries (see Figure 10(b) blue arrow). Four points, two on each side, with maximum slopes that are close to the section with maximum curvature, are chosen as candidates for hilum end points (see Figure 10(b), A, B, C, D). Two of those points are selected to be the hilum end points by using heuristic rules. The rules use, among other information, the relative position of the points with respect to the medial axes.

3.6 Lung root detection

Generally, the root of the lung is understood to be the entire hilum surface, where many structures enter or leave the lung (Betke *et al.*, 2003). However, we need a more specific definition of the lung root to use it as a landmark for other image analyses. After discussions with radiologists, the point where the main bronchus passes through the hilum surface is chosen to represent the lung root. Figure 10(d) illustrates the lung root point, which is the midpoint of the first intersection between the bronchi and the hilum surface.

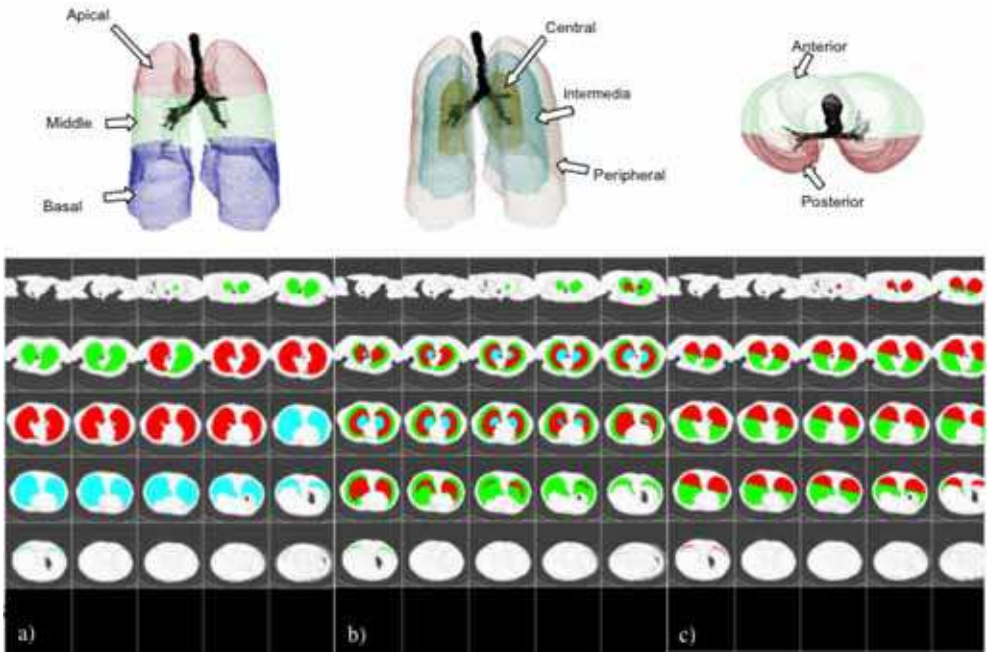

Fig. 11. Lung regions in 3D and projected on 2D axial images. Lung division into: apical, middle, basal (a), central, intermediate, peripheral (b) and anterior, posterior (c).

3.7 Dividing lung into pulmonary regions

A novel approach for dividing the lung and parenchyma into multiple clinically meaningful regions is as follows. The entire lung parenchyma is divided into three axes: apical-middle-basal, anterior-posterior and peripheral-intermediate-central, which creates eight overlapping regions. For the purpose of HRCT image integration, the lung regions are mapped to each 2D axial image.

Each lung is vertically divided into *apical*, *middle* and *basal* regions. The images above the hilum belong to the *apex* of the lung, the images in the region of hilum belong to the *middle* region of the lung and the images bellow the hilum belong to the *base* of the lung. Figure 11(a) shows an example of the apical-basal division. The apical, middle, and basal regions in 2D are displayed in green, red, and blue colour, respectively.

The coronal plane, which runs through the centre of the carina, is used to divide the lung into two parts: *anterior* and *posterior*. However, not all HRCT scans are taken in a perfectly prone-supine orientation (i.e. the subject does not lie perfectly flat). Two additional landmarks, namely the *spinal cord* and *sternum*, are used for the alignment. The coronal plane needs to be perpendicular to the medial plane that runs through the centre of the spinal cord and the sternum. An example of the resulting anterior-posterior division is shown in Figure 11(c). The anterior and posterior regions are displayed in green and red colour, respectively.

To divide the lung into *central*, *medial* and *peripheral* regions, the following 3D algorithm, developed together with a radiologist from our group, was used. A three-dimensional position of the lung root and voxels belonging to the lung surface are used. For each lung, a line is drawn between the lung root and each lung surface voxel. Since the lung root is outside the lung, the line will pass the lung surface twice, in and out. The line section between the first and the second crossing points are then divided into three parts equally. The first part, closer to the lung root, is the *central* region, the second part is *intermediate* region and the last third is *peripheral* region. The central, intermediate and peripheral divisions are projected onto 2D axial images (Figure 11(b)). After segmenting the anatomy, landmarks and lung regions, the images are prepared for detecting abnormal findings.

4. Computer-aided detection and interpretation of disease patterns

There is a substantial number of different disease patterns that can be visually identified in HRCT images of the lungs. In this chapter, we report on the detection of two kinds. One shows structural deformation of the bronchi by bronchial dilatation and bronchial wall thickening and the other shows fibrous changes of the lung parenchyma, represented by honeycombing. Bronchial dilatation and bronchial wall thickening patterns are associated with Bronchiectasis and honeycombing is associated with Interstitial Diffuse Lung Diseases (IDLD) or Diffuse Parenchymal Lung Disease (DPLD). The two examples described here were chosen to demonstrate the different detection techniques required by different disease patterns.

Rules for classifying the detected patterns were built automatically using supervised machine learning. In supervised learning, a set of pre-classified training examples is used to generate classification rules. We used J48, the Weka (Witten *et al.*, 2005) implementation of the C4.5 decision tree induction algorithm. The input to J48 was a set of classified examples of disease patterns represented by a set of image attributes. The result of learning is a classification tree in which the most informative attributes are used to determine the correct class.

4.1 Bronchial dilatation as a direct sign for Bronchiectasis

Bronchiectasis is defined as localised, irreversible bronchial dilatation, often with thickening of the bronchial wall (Webb, et al., 2000). Dilation of a bronchus is detected by comparing its size with the size of the accompanying artery. Bronchiectasis is considered present when the internal diameter of a bronchus is greater than that of the adjacent pulmonary artery. The typical appearance of this pattern is known as the "signet ring sign" (see Figure 8). Webb *et al*. (2000) reported that subjective visual criteria are most often used in the interpretation of HRCT images and a few different scoring systems are used to assess bronchaectasis extend and severity. We have used an HRCT bronchiectasis scoring system (Webb *et al.*, 2000) that provides ranges for bronchial dilatation and the bronchial wall thickening.

A set of parameters, calculated to compare the bronchus and its accompanying artery, includes lumen area, shortest diameter and the ratios of the lumen areas and the shortest diameters of a broncho-vascular pair.

Machine learning was used to automatically determine the severity thresholds and to determine which parameters to use in assessing the severity for different sizes of bronchi (Zrimec *et al*., 2003; Busayarat & Zrimec, 2005). Figure 12 shows radiologist's marked examples of bronchial dilatation and results of the detected and classified by a computer.

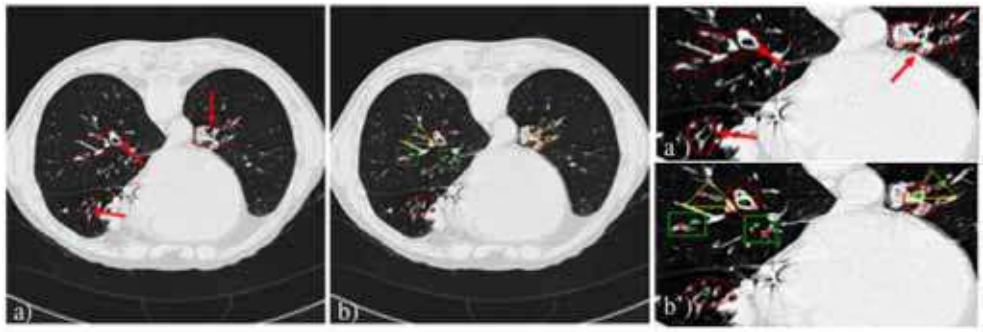

Fig. 12. Results of bronchial dilatation detection and severity assessment. Radiologist's marked broncho-arterial pairs (a), red arrows dilated (a'); computer detection results with severity assessment (b), green rectangle: normal, yellow triangle: mild dilatation (b').

4.2 Honeycombing as a sign for interstitial lung diseases

Honeycombing indicates a disease process characterised by a cluster of air-filled cysts divided by thick walls. The cysts range from a few millimetres to several centimetres and occur predominantly in the periphery of the lung (Webb, et al., 2000). Honeycombing is common in patients with idiopathic pulmonary fibrosis (IPF) and other interstitial diseases. In an HRCT image, honeycombing can be seen as a cluster of roughly circular dark patches surrounded by white walls (see Figure 13). Because of its characteristic appearance, honeycombing is a challenging pattern to detect by a computer. For example, broncho-vascular structures have similar appearance (see Figure 13).

Honeycombing is present in many disorders that primarily affect the lung parenchyma. They are characterised by specific abnormal findings, mostly texture-like in appearance. Consequently, most of the automated detection algorithms, being developed to analyse CT scans are texture based. The classical approach is to use a set of image features to describe

the image content and to use some classification scheme to distinguish between different patterns. Initially, we adopted a similar approach. After experimenting with different attribute subsets for describing the content of the image and with different learning schemes for improving the system's performance, the results reveal that classical pattern detection approaches do not perform satisfactorily. The problem is that texture descriptors, alone, do not capture information that is pertinent to medical images, i.e. the disease appearance and distribution. Therefore, we incorporated knowledge of the lung regions and anatomy as well as specialist's knowledge of disease appearance, which help improve the detection.

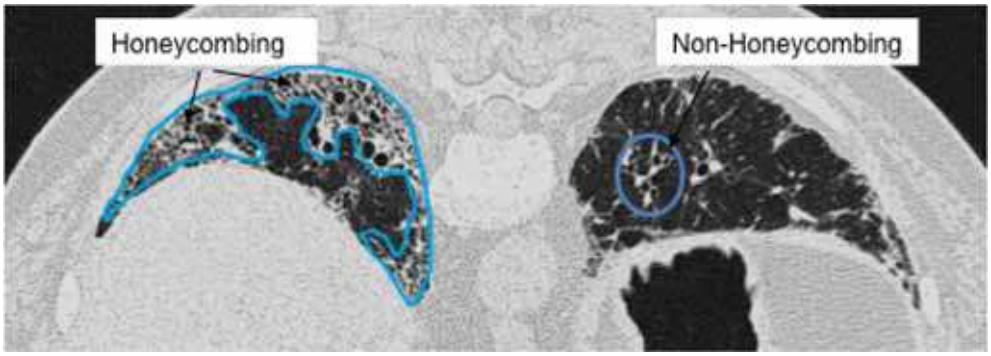

Fig. 13. Left lung - outlined region with honeycombing. Right lung - outlined example of broncho-vascular structures, which has similar appearance as honeycombing.

Rules for discriminating between honeycombing and non-honeycombing patterns were created automatically by supervised machine learning. The training examples were obtained from the images with labelled regions provided by radiologists. The regions with representative examples of honeycombing and other lung diseases patterns, marked by the radiologists as described in section 2.3, were processed to extract statistical features from the images that best represent the underlying texture. The marked regions were subdivided into blocks of size 7x7 and 15x15 pixels. Adjacent blocks overlapped such that the centres of adjacent blocks were three pixels apart. A set of attributes was calculated for each central pixel and it's neighbours in the block. Two block sizes were used to capture the characteristics of small and larger honeycombing cysts.

First and second order texture attributes and grey-level difference were calculated for each block (Haralick, 1979; Wong & Zrimec, 2007). The first order texture attributes measure the grey-level distribution within the block. Those attributes include: the mean HU, variance, skewness, kurtosis, energy and entropy. The second order features describe the spatial distribution of the grey-levels within these blocks. A co-occurrence matrix is calculated that specifies the frequency of a particular grey-level occurring near another grey-level. The co-occurrences of the grey-levels for four different directions were measured: 0^o, 45^o, 90^o, 135^o. Each pixel, with its surrounding area, is represented by 63 attributes per window, resulting in a feature vector with 126 attributes (63 for blocks of 7x7 pixels and 63 for blocks of 15x15pixels).

Correlation-based Feature Selection (CFS) (Hall, 2000) was used to reduce the dimensionality of the feature vector. CFS selects subsets of attributes that are highly correlated with the class and that have low inter-correlation.

A subset of features that best discriminates honeycombed and non-honeycombed regions was selected and used for learning. J48 decision tree learning produced rules for recognising honeycombing regions. Figure 14(a) shows an example of applying the classification rules.
We used expert knowledge about the appearance of honeycombing to improve the classification results. An example of such knowledge is that "Honeycombing results in cysts …which have a peripheral predominance" (Webb, at al., 2000. pp 91). We implemented a post-processing step using knowledge about the lung regions (section 3.7). Masks with peripheral, intermediated and central regions were used to guide the classification algorithm. The classification algorithm classifies potential blocks as honeycombing only if they are in the periphery of the lung or in close proximity to other blocks classified as honeycombing. Results of the detection are shown in Figure 14, which contains the original image (Fig 14(a)), image with overlaid lung regions (Fig 14(b)), to determine the lung periphery, and regions with detected honeycombing (Fig 14(c)).

5. Results

Results of the methods developed to detect abnormalities in airways indicating Bronchiectasis and honeycombing are presented. The performance was compared against the manual reference set using the following three measures:

$$accuracy = \frac{TP + TN}{P + N} \quad sensitivity = \frac{TP}{TP + FN} \quad specificity = \frac{TN}{TN + FP} \quad precision = \frac{TP}{TP + FP}$$

where TP is the true positive rate, i.e., the number of pixels correctly classified. TN is true negative rate. FP is the false positive rate and FN is false negative rate. P and N indicate the total number of positives and the number of negatives. A*ccuracy* is the degree of closeness of measurements of a quantity to its actual (true) value. *Sensitivity* determines the proportion of actual disease pattern that has been detected. *Specificity* measures the amount of non-disease pattern that has been classified as non-disease pattern. *Precision* - reproducibility or repeatability is the degree to which repeated measurements under unchanged conditions show the same results.

5.1 Evaluation of the success of detection of bronchial dilation and bronchial wall thickening singes

The success of the disease patterns detection depends on quality of feature segmentation. This evaluation consisted of the following experiments:

- the success of the automatic segmentation of bronchi,
- the success of correctly identified broncho-arterial pairs,
- the success of detection of the extent of baronial dilatation,
- the success of detection of bronchial wall thickening.

The result of the automatic detection of bronchi was compared with the 711 manually identified bronchi from 67 images of 18 subjects. It achieved 73% sensitivity and 83% accuracy on the unseen data. Most of the false negatives occur with small bronchi, which radiologists also have difficulty in identifying.
The experiment for evaluating artery detection and bronchial-dilatation assessment was performed on 324 HRCT images from 64 subjects. Ground truth or the reference set consisted of 442 broncho-arterial pairs manually marked and verified by experienced

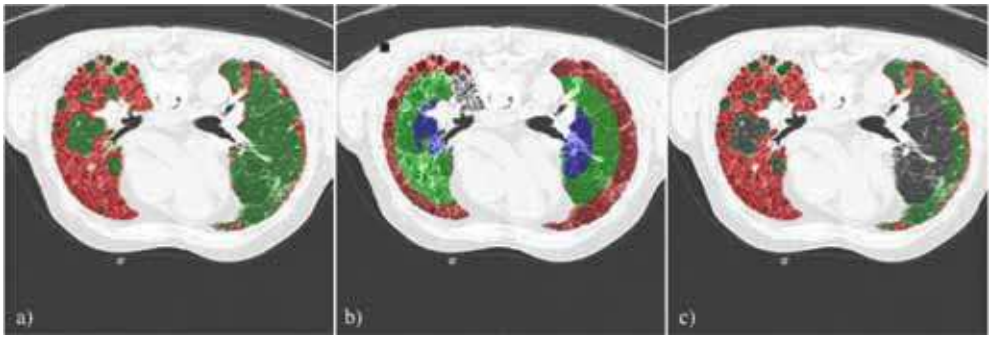

Fig. 14. Results of honeycombing detection (a) (red – honeycombing and green – non-honeycombing), image with regional information (b), final results after post processing (c).

radiologist PW. The artery detection was considered as correct if the centre was detected with error < 2 pixels. Artery detection achieved 90% accuracy (400/442). Figures 12(b) and 12(b') show the results of the broncho-arterial pairs detection.

To evaluate the performance of the severity of the bronchi dilation, 194 broncho-arterial pairs were manually classified as normal (94), mild (64) or severe (36). The experiment for baronial dilatation assessment only used samples that have correctly detected arteries. On 10-fold cross-validation, the system achieved 82% accuracy.

Bronchial wall thickening was evaluated on 12 broncho-arterial pairs marked by radiologists. The system demonstrated 83% correct detection. Examples of bronchial wall thickening and severity assessment are shown in Figure 15.

5.2 Evaluation of honeycombing detection

The performance of rules generated by machine learning is tested by cross-validation and by applying them to previously unseen cases. This evaluation consisted of the following experiments:

- Creation of the classifier and evaluation of its performance with 10 fold cross validation;
- Evaluation the success of classifying unseen cases.

The detection of honeycombing was tested on 42 HRCT images from 10 patients. The training data set consisted of 30 images with 110 marked and labelled regions by radiologists. Those regions were used to generate 2964 blocks with honeycombing and 2569 blocks with non-honeycombing training examples. Using tenfold cross validation, the method achieved 98% accuracy.

A set of 12 unseen images was used for evaluation. In the evaluation set, there were 28 regions with honeycombing and 20 regions without honeycombing. This resulted into 1240 blocks with honeycombing and 876 blocks with non-honeycombing regions. The evaluation on the unseen data achieved 94.6% accuracy. The evaluation was performed on the radiologist's marked regions.

6. Discussion

To validate the robustness of the algorithm in real clinical practice, the dataset is selected to have variations that reflect the real data. There are variations in four difference aspects: number of slices, slice gap, slice thickness and spatial pixel size. The slice gap, or distance

between two adjacent slices, in our data set is a constant of 15 milimeters. Another aspect we considered was the variety of patients. The dataset was selected to include scans with a wide range of abnormalities. In particular, it includes subjects with high-density abnormalities, such as ground glass opacity, and with low-density abnormalities, such as emphysema. It also includes a few cases of airways abnormalities, such as bronchiectasis.

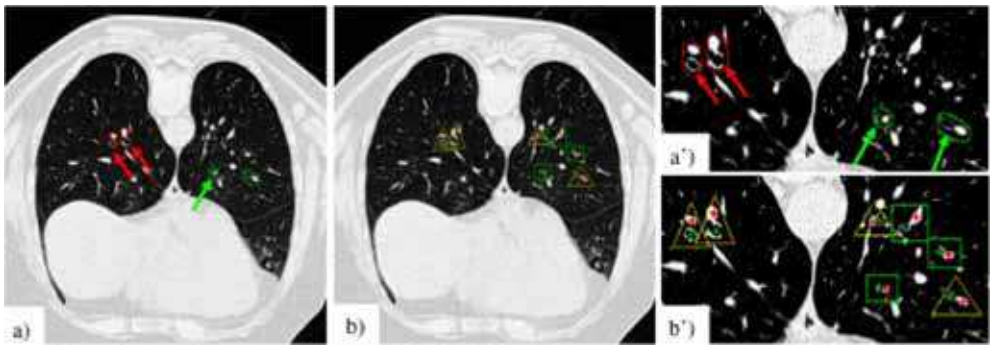

Fig. 15. Results of bronchial wall thickening detection and severity assessment. Radiologist's marked broncho-arterial pairs (a), green arrows - normal and red arrows dilated (a'); computer detection results with severity assessment (b), green rectangle: normal, yellow triangle: mild dilatation (b').

To evaluate the performance of the segmentation algorithms a set of scans from 84 subjects was used. Each scan contained a series of cross-sectional images in the axial plane. There were a total number of 1685 images. The evaluation was performed on a manually segmented data set, verified by a radiologist. The evaluation showed that the segmentation algorithms were quite successful with the sensitivity shown in Table 1. From the results presented in Table 1, we can see that the chosen landmarks are very stable across patients.

Our segmentation algorithms have mostly been developed for processing two-dimensional axial images rather than 3D because the radiology practices that supplied the data routinely use images with 15 mm gaps for analysing diffuse interstitial lung diseases. There is a trend, in the recent years, to move from two-dimensional to three-dimensional processing (Sluimer, 2005). A three-dimensional data set is necessary for bronchial and arterial three segmentation and we have already experimented on a limited data set of 20 subjects to segment both structures.

A major problem in the evaluation was the creation of a reference dataset, which required manual tracing of outlines. To assist in the creation of the reference dataset, we developed interactive tools for annotating regions, lines and points in the images that represent anatomical structures (Rudrapatna, et al., 2004) . The reference standard or the ground truth, used for evaluating the anatomy segmentation was manually created by an observer who is familiar with lung anatomy. The reference standard was verified and corrected by three expert radiologists to ensure accuracy of the data. These tools enforce consistency of manual segmentation amongst radiologists. The same tools can be used in clinical practice for manually correcting cases where the automatic segmentation was not successful.

The tasks of detecting, classifying and labelling possible disease patterns were demonstrated on two kinds of diseases patterns, one related to structural deformation of the bronchial tree

and one showing fibrotic changes of the lung parenchyma. The results show that the system is able to recognise potential lung abnormalities and indicate their size and location. Computer analysis and evaluation of bronchial morphology, especially bronchial thickness, is important, because bronchi are responsive to treatment. This system can help assess treatment outcomes as well as assist in studies of the effects of new drugs.
Differential diagnosis in the case of interstitial lung disease is difficult even for experienced chest radiologists. Radiologists inspect the appearance of lung regions in all images and based on the pattern of pathology and its distribution, along with the patient's history, an evaluation of the case is reported. Although the current system does not have access to the patient's history we have preliminary results from automated methods for calculating the percentage of affected lung and for assessing the distribution of the decease patterns. The system provides a list of possible diagnoses with their probability, based on the patterns detected in the images. Radiologists then combine the suggested differential diagnosis with the patient history for the case report.

7. Conclusions and future work

We have presented a system for computer-aided detection of disease patterns. In the proposed framework, normal anatomy and anatomical landmarks are segmented and used to detect disease patterns. Recognising normal anatomy helps in detecting many diseases that have similar appearance. For example, the appearance of honeycombing is similar to normal bronchi and vessels. Because we know the expected location of the bronchi and vessels, they can be eliminated, leaving the honeycombing. Most of the methods developed are knowledge-guided. Knowledge of anatomy comes from a model of the lung. Specific knowledge, related to HRCT images, was acquired via machine learning from examples. Knowledge about disease appearance and its distribution in the lungs was encoded in heuristic rules. Having learned the lung anatomy and having developed a model of the lung, we are now concentrating on building systems for recognising patterns created by other lung diseases.

Landmark	Trachea	Carina	Sternum	Spinal Cord	Hilum
%Sensitivity	100%	99%	99%	96%	93%

Table 1. Results of the automatic segmentation of anatomical landmarks.

Although there is an increasing number of publications on computer added CT analysis of DILD, it is difficult to compare the results form different groups. One of the problems is the absence of a common, carefully annotated and representative database for benchmarking algorithms (Sluimer, 2005) similar to the Lung Image Database Consortium for nodule detection (Armato *et al.*, 2004). We are already making efforts in developing similar data sets for interstitial lung diseases detection.

8. Acknowledgment

We thank Claude Sammut for his comments and Medical Imaging Australia for providing images. We also thank radiologists Peter Wilson, Michael Jones Daniel Moses and Pravati Panigrahi for providing clinical resources, image annotation and inspection of the results.

9. References

Archip, N., Erard, P. J., Egmont-Petersen, M., Haefliger, J. M., & Germond, J. F. (2002). A knowledge-based approach to automatic detection of the spinal cord in CT images. IEEE Transactions on Medical Imaging, pp. 1504-1515.

Armato, S. G., & Sensakovic, F. W. (2004). Automated lung segmentation for thoracic CT. Academic Radiology , 11 (9), 1011-1021.

Armato SG, McLennan G, McNitt-Gray MF, et al. (2004). The Lung Image Database Consortium: developing a resource for the medical imaging re- search community. Radiology 2004; 232:739–748.

Aykac, D., Hoffman, E. A., McLennan, G., & Reinhardt, J. M. (2003). Segmentation and analysis of the human airway tree from three-dimensional X-Ray CT images. IEEE Transactions on Medical Imaging, 2(8), 940-950.

Betke, M., Hong, H., Thomas, D., Prince, C., & Ko, J. (2003). Landmark detection in the chest and registration of lung surfaces with an application to nodule registration. Medical Image Analysis , 7, 265–281.

British Thoracic Society, (1999). BTS guidelines on the diagnosis, assessment and treatment of diffuse parenchymal lung disease in adults, Thorax, vol. 54, no. Supplement 1, pp. S24–S30.

Brown, M. S., McNitt-Gray, (2000). Medical Image Interpretation, Handbook of Medical Imaging, Volume 2. Medical Image Processing and Analysis, ISBN 9780819477606, SPIE Press, 399-440.

Brown, M. S., McNitt-Gray, M. F., Mankovich, N. J., Goldin, J. G., Hiller, J., Wilson, L. S., et al. (1997). Method for segmenting chest CT image data using an anatomical model: Preliminary results. IEEE Transaction on Medical Imaging , 16 (6), 828-839.

Busayarat, S., & Zrimec, T. (2005a). Knowledge-directed automatic bronchi detection method for sparse HRCT scans of the lungs. Image and Vision Computing New Zealand, (pp. 369-374).

Busayarat, S., & Zrimec, T. (2005b). Automatic detection of pulmonary arteries and assessment of bronchial dilatation in HRCT images of the lungs. Computational Intelligence: Methods & Applications, Istanbul, pp. 5-10.

Chiplunkar, R., Reinhardt, J. M., & Hoffman, E. A. (1997). Segmentation and quantitation of the primary human airway tree. Society of Photographic Instrumentation Engineers- Medical Imaging, SPIE 3033, pp. 403-414.

Chabat, F., Hu, X., Hansell, D. M., & Yang, G.-Z. (2001). ERS transform for the automated detection of bronchial abnormalities on CT of the lungs. IEEE Transactions on Medical Imaging , 20 (9), 942-952.

Depeursinge, A., (2010). Affine–invariant texture analysis and retrieval of 3D medical images with clinical context integration, Phd Thesis, Unicersity Geneva.

Depeursinge, A., de Ville, D. V., Unser, M. , & M¨uller, H.(2008). Lung tissue analysis using isotropic polyharmonic B-Spline wavelets. In MICCAI ’08: Proceedings of the First International Workshop on Pulmonary Image Analysis, New York, September, Springer, pp.125–133.

Depeursinge, A., Iavindrasana, J. , Hidki, A., Cohen, G., Geissbuhler, A., Platon, A., Poletti, P.-A. & M¨uller, H. (2008). A classification framework for lung tissue categorization. In K. P. Andriole and K. M. Siddiqui, editors, Medical Imaging 2008: PACS and Imaging Informatics, SPIE 6919, pp. 69190C- 69190C12.

Deglint, H. J., Rangayyan, R. M., Ayres, F. J., Boag, G. S., & Zuffo, M. K. (2007). Three-dimensional segmentation of the tumor in computed tomographic images of neuroblastoma. Digital Imaging , 20 (1), 72-87.

Eenakshi, S., Manjunath, K.Y., Balasubramanyam, V. (2004). Morphological variations of the lung fissures and lobes, Indian J. Chest Dis. Allied Sci., Vol. 46(3): 179-182.

Fetita, C., & Preteux, F. (1999). Three-dimensional reconstruction of human bronchial tree in HRCT. Proceedings of the International Society for Optical Engineering, *3646*, pp. 281-29.

Fetita, C., & Preteux, F. (2000). Bronchial tree modeling and 3D reconstruction. Society of Photographic Instrumentation Engineers, pp. 16-29.

Fetita, C., & Preteux, F. (2001). CT data-driven 3D airway model synthesis. World Multi Conference on Systemics, Cybernetics and Informatics, pp. 111-116.

Garnavi, R., Baraani-Dastjerdi, A., Moghaddam, H. A., Giti, M., & Rad, A. A. (2005). A new segmentation method for lung HRCT images. Digital Image Computing on Techniques and Applications, (p. 52).

Gonzalez, R. C., & Woods, R. E. (1993). Digital image processing. Addison Wesley.

Hall, M. A. (2000). Correlation-based feature selection for discrete and numeric class machine learning. In: ICML '00: Proceedings of the Seventeenth International Conference on Machine Learning, San Francisco, CA, USA, Morgan Kaufmann Publishers Inc. pp. 359–366.

Haralick, R. M., (1979). Statistical and Structural Approaches to Texture, Proceedings of the IEEE 67, pp. 786– 804.

Hu, S., Hoffman, E. A., & Reinhardt, J. M. (2001). Automatic lung segmentation for accurate quantitation of volumetric X-ray CT images. IEEE Transcation on Medical Imaging, 20 (6), 490-498.

Jain, R., Kasturi R. & Schunk, B. (1995). Machine vision, McGraw Hill.

Kass, M., Whitkin, A., & Terzopoulos, D. (1987). Snakes: active contour models. Proceedings of 1st International Conference on Computer Vision, London, pp. 259-269.

Kubo, M., Kawata, Y., Niki, N., Eguchi, K., Ohmatsu, H., Kakinuma, R., et al. (2001). Automatic extraction of pulmonary fissures from multidetector-row CT images. Internation Conference on Image Processing IEEE, pp. 1091-1094.

Kuhnigk, J. M., Dicken, V., Zidowitz, S., Bornemann, L., Kuemmerlen, B., Krass, S., et al. (2005). New tools for computer assistance in thoracic CT. part 1. functional analysis of lungs, lung lobes, and bronchopulmonary segments. Radio Graphics , 25, 525-536.

Lathi, B. P. (1998). Singal processing and linear systems. Berkeley-Cambridge.

Li, B. (2004). The construction of a normative human lung atlas by inter-subject registration and warping of CT images. PhD Thesis, University of Iowa.

Li, B., & Reinhardt, J. M. (2001). Automatic generation of object shape models and their application to tomographic image segmentation. Society of Photographic Instrumentation Engineers, 4322, pp. 311-322.

Madden, M. E. (2001). Introduction to sectional anatomy. Lippincott Williams & Wilkins.

Moore, K., & Dalley, A. (1999). Clinically oriented anatomy. Lippincott Williams and Wilkins.

Muller, N. (1991), Clinical value of High-Resolution CT in chronic diffuse lung disease, American Journal of Roentgenology, vol. 157, pp. 1163-1170.

Papalousis, J. (2003). LMIK – Anatomy and lung measurements using active contour snakes. Undergraduate Thesis, University of New South Wales.

Preteux, F., Fetita, C., & Grenier, P. (1997). Modeling, segmentation, and caliber estimation of bronchi in high-resolution computerized tomography. Society of Photographic Instrumentation Engineers, 3026, pp. 58-69.

Rudinsky, S., & Smirniotopoulos, J. G. (2006), Retrieved September 23 from Radiology glossary: http://rad.usuhs.mil/glossary.html

Rudrapatna, M., Sowmya, A., Zrimec, T., Wilson, P., Kossoff, G., Wong, J., Busayarat, S. , Misra, A., Lucas, P. (2004). LMIK – Learning Medical Image Knowledge: An Internet-based medical image knowledge acquisition framework", Electronic Imaging Science and Technology, IS&T/SPIE's 16th Annual Symposium, Jan 2004, San Jose, CA.

Shapiro, L., & Stockman, G. (2001). Computer vision. Prentice Hall.

Sluimer, I. C. (2005). Automated image analysis of the pathological lung in CT. PhD Thesis, Utrecht University.

Sonka, M. (2000). Handbook of medical imaging, volume 2. medical image processing and analysis. SPIE.

Suetens, P. (2008). Fundamentals of medical imaging. Second Edition, Cambridge University Press.

Tschirren, J., Palagyi, K., Reinhardt, J. M., Hoffman, E. A., & Sonka, M. (2002). Segmentation, skeletoniztion, and branchpoint matching -- a fully automated quantitative evaluation of human intrathoracic airway trees. Medical Image Computing and Computer-Assisted Intervention. Springer, 2489, pp. 12-19.

Tolouee, A., Abrishami-Moghaddam, H., Garnavi, R., Forouzanfar, M., & Giti, M. (2008). Texture analysis in lung HRCT images. 2008 Digital Image Computing: Techniques and Applications, dicta, pp.305-311.

Uchiyama, Y., Katsuragawa, S., Abe, H., Shiraishi, J., Li, F., Li, Q., Zhang, C.-T., Suzuki, K., and Doi, K. (2003). Quantitative computerized analysis of diffuse lung disease in high-resolution computed tomography", Medical Physics, Vol. 30(9): 2440–2454.

Uppaluri, R., Hoffman, E. A., Sonka, M., Hartley, P. G., Hunninghake, G.W., & McLennan, G. (1999). Computer recognition of regional lung disease patterns", American Journal of Respiratory and Critical Care Medicine, 160 (2): pp. 648–654.

Wang, J., Betke, M., & Ko, J. P. (2006). Segmentation of pulmonary fissures on diagnostic CT. Medical Image Analysis , 10, 530.

Webb, R. W., Muller, N., & Naidich, D. P. (2000). High-resolution CT of the lung, third edition. Lippincott Williams & Wilkins.

Witten, I.H., & Frank, E., (2005). Data mining: practical machine learning tools and techniques, Morgan Kaufmann Series in Data Management Sys, Morgan Kaufmann, second ed., June.

Wong, J., & Zrimec, T. (2007). Efficient detection of diffuse lung disease. Medical Imaging 2007: Computer-Aided Diagnosis Maryellen L. Giger; Nico Karssemeijer, Editors, SPIE Vol: 6514, pp. 651425-651431

Zhang, L., & Reinhardt, J. M. (1999). Detection of lung lobar fissures using fuzzy logic. Society of Photographic Instrumentation Engineers-Medical Imaging , 3660, 188-198.

Zhang, L., Hoffman, E. A., & Reinhardt, J. M. (2003). Atlas-driven lung lobe segmentation in volumetric x-ray CT images. SPIE. 5031, p. 308.

Zrimec, T., & Busayarat, S. (2004). 3D modelling and visualization of the human lung. Proceedings of the 2nd International Symposium on 3D Data Processing: Visualization and Transmission, pp. 110-115.

Zrimec, T., & Wong, J. (2007). Methods for automatic honeycombing detection In Hrct images of the lung. Mediterranean Conference on Medical and Biological Engineering (pp. 830-833). Springer, pp. 830-833.

Zrimec, T., Busayarat, S., & Wilson, P. (2004). A 3D model of the human lung. Proceedings of the International Society and Conference Series on Medical Image Computing and Computer-Assisted Intervention Springer, pp. 1074–1075.

Zrimec, T., Busayarat, S., & Wilson, P. (2003). A knowledge based approach for automatic detection and measurement of bronchial dilatation and Wall Thickening on HRCT Images of the Lungs. World Congress on Medical Physics and Biomedical Engineering. Springer, Sydney.

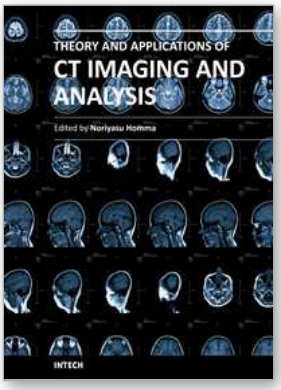

Theory and Applications of CT Imaging and Analysis
Edited by Prof. Noriyasu Homma

ISBN 978-953-307-234-0
Hard cover, 290 pages
Publisher InTech
Published online 04, April, 2011
Published in print edition April, 2011

The x-ray computed tomography (CT) is well known as a useful imaging method and thus CT images have continuingly been used for many applications, especially in medical fields. This book discloses recent advances and new ideas in theories and applications for CT imaging and its analysis. The 16 chapters selected in this book cover not only the major topics of CT imaging and analysis in medical fields, but also some advanced applications for forensic and industrial purposes. These chapters propose state-of-the-art approaches and cutting-edge research results.

How to reference
In order to correctly reference this scholarly work, feel free to copy and paste the following:

Zrimec Tatjana and Sata Busayarat (2011). Computer-aided Analysis and Interpretation of HRCT Images of the Lung, Theory and Applications of CT Imaging and Analysis, Prof. Noriyasu Homma (Ed.), ISBN: 978-953-307-234-0, InTech, Available from: http://www.intechopen.com/books/theory-and-applications-of-ct-imaging-and-analysis/computer-aided-analysis-and-interpretation-of-hrct-images-of-the-lung

INTECH
open science | open minds

InTech Europe
University Campus STeP Ri
Slavka Krautzeka 83/A
51000 Rijeka, Croatia
Phone: +385 (51) 770 447
Fax: +385 (51) 686 166
www.intechopen.com

InTech China
Unit 405, Office Block, Hotel Equatorial Shanghai
No.65, Yan An Road (West), Shanghai, 200040, China
中国上海市延安西路65号上海国际贵都大饭店办公楼405单元
Phone: +86-21-62489820
Fax: +86-21-62489821